

ELECTROCHEMISTRY

Tantalum-stabilized ruthenium oxide electrocatalysts for industrial water electrolysis

Jiahao Zhang^{1,2†}, Xianbiao Fu^{2†}, Soonho Kwon^{3†}, Kaifeng Chen⁴, Xiaozhi Liu⁵, Jin Yang⁶, Haoran Sun⁶, Yanchang Wang⁷, Tomoki Uchiyama⁷, Yoshiharu Uchimoto⁷, Shaofeng Li⁸, Yan Li⁹, Xiaolong Fan¹⁰, Gong Chen¹¹, Fanjie Xia¹², Jinsong Wu¹², Yanbo Li², Qin Yue², Liang Qiao⁴, Dong Su⁵, Hua Zhou⁹, William A. Goddard III^{3*}, Yijin Kang^{1*}

The iridium oxide (IrO₂) catalyst for the oxygen evolution reaction used industrially (in proton exchange membrane water electrolyzers) is scarce and costly. Although ruthenium oxide (RuO₂) is a promising alternative, its poor stability has hindered practical application. We used well-defined extended surface models to identify that RuO₂ undergoes structure-dependent corrosion that causes Ru dissolution. Tantalum (Ta) doping effectively stabilized RuO₂ against such corrosion and enhanced the intrinsic activity of RuO₂. In an industrial demonstration, Ta-RuO₂ electrocatalyst exhibited stability near that of IrO₂ and had a performance decay rate of ~14 microvolts per hour in a 2800-hour test. At current densities of 1 ampere per square centimeter, it had an overpotential 330 millivolts less than that of IrO₂.

Water electrolysis driven by renewable power sources is an important route for green hydrogen production (1). Unfortunately, the sluggish kinetics, low efficiency, and excess energy consumption required for oxygen evolution reaction (OER) make OER the bottleneck for high-efficiency water electrolysis (2, 3). Proton-exchange membrane water electrolysis (PEM-WE) is the most attractive among all water electrolysis technologies for its high current density (and hence high hydrogen production rate), high purity, and high pressure for hydrogen output and quick response that enables ready coupling with renewable power sources (4, 5). However, the harsh operating environment (high acidity and high potential) of OER electrocatalysts poses severe requirements in chemical stability for PEM-WE (6–8). Although many new OER electrocatalysts have been discovered (8–20), the PEM-WE industry still primarily uses first-

generation iridium oxide (IrO₂), which is limited for large-scale applications by the extreme scarcity and high cost of Ir (21, 22). Additionally, although the stability of IrO₂ meets current industrial requirements, the activity of IrO₂ OER electrocatalysts must be dramatically improved to enable competitive hydrogen production.

Ruthenium oxide (RuO₂), the second-most attractive option for OER catalysts, offers advantages, including the relatively high reserves and low cost of Ru compared with Ir, as well as high activity (23–26). However, the poor stability of RuO₂ prevents practical applications. The Faradaic efficiency of Ru dissolution for RuO₂ electrocatalysts in the normal operation of water electrolysis is ~0.1%, which is at least two orders of magnitude higher than that of the Ir dissolution in IrO₂ catalysts. To improve the performance of RuO₂, it is crucial to identify new modified materials that extend the structure-property correlation for both activity and stability, as well as to establish the reaction mechanism. For example, many studies suggest that lattice oxygen exchange is involved in the OER process and is responsible for the dissolution of RuO₂ catalysts (17, 18, 27), whereas others claim lattice oxygen exchange is not observed (28). Mixing tantalum pentoxide (Ta₂O₅) and RuO₂ (or IrO₂) has led to slightly improved stability (29, 30), but this approach has not been further explored.

In this study, we examined well-defined extended surfaces of RuO₂ with selected crystalline orientations to investigate the structure-property correlations in OER. We identified structure-dependent corrosion of RuO₂ as responsible for both low stability and low activity. However, we found that doping Ta into RuO₂ both enhanced the intrinsic activity of RuO₂ toward OER and suppressed RuO₂ corrosion, while also alleviating Ru dissolution in water electrolysis, dramatically improving electrocatalyst stability. To understand the atomistic origin of

how Ta improved performance and stability, we performed grand canonical quantum mechanics (GCQM) calculations (31) to describe the mechanism and stability as a function of applied potential. Based on what we learned from these QM and experimental studies on the well-defined extended surface of RuO₂, we synthesized nanoparticulate Ta-RuO₂ electrocatalysts and demonstrated performance in an industrial-scale membrane electrode assembly (MEA). Moreover, a full industrial demonstration showcased hydrogen production from solar energy at up to megawatt rates to feed a hydrogen refueling station.

Well-defined extended surface of RuO₂

RuO₂ films were prepared by pulse laser deposition (demonstrated in supplementary materials, materials and methods). The films used in our experiments showed similar thickness and root mean square (RMS) roughness according to x-ray reflection (XRR) (fig. S1) and atomic force microscopy (fig. S2 and table S1). Before the OER experiments, we examined the cathodic pseudocapacitive charge, q^*_{cathodic} (32, 33), of the thin films to determine the population of available electrochemically active sites (fig. S3A and table S2). Because RuO₂ extended surfaces with different orientations have different surface atomic arrangements (Fig. 1A, insets), the number of coordinatively unsaturated sites (CUS) of Ru for various surfaces is expected to be different. We calculated the CUS as 10 nm⁻² for (001), 7 nm⁻² for (100), 5 nm⁻² for (110), and 7 nm⁻² for (111). As shown in Fig. 1B, the measured cathodic charge densities showed a good linear correlation with a Pearson correlation coefficient of 0.91 to the CUS Ru numbers [which is consistent with previous reports (28)], indicating that the surface-exposed Ru atoms were available for electrochemical reactions.

The OER properties of RuO₂ thin films were evaluated first by cyclic voltammetry (CV), as shown in fig. S4. The OER current densities of pristine RuO₂ surface correlated strongly with the charge density, q^*_{cathodic} , indicating that the population of Ru sites was a dominant factor for the overall OER activity of RuO₂ thin films (Fig. 1C). We note the electrochemical properties of RuO₂ thin films that changed after CV cycling: Although (001), (110), and (100) surfaces showed an apparent activation process, the (111) surface exhibited a decay in current density over time but no activation barrier (fig. S4).

We used x-ray diffraction (XRD) to examine the thin films after 10 cycles of CV to understand the changes in electrode performance (Fig. 1D). Two new XRD peaks at 21.2° and 23.6° appeared on all thin films regardless of orientation. The best match for the new peaks is RuO₄ [monoclinic, C2/c (15)], which has been suggested to be involved in the corrosion process of RuO₂. (34, 35). We calculated the

¹School of Chemical Engineering, Sichuan University, Chengdu, China. ²Institute of Fundamental and Frontier Sciences, University of Electronic Science and Technology of China, Chengdu, China. ³Materials and Process Simulation Center, California Institute of Technology, Pasadena, CA, USA. ⁴School of Physics, University of Electronic Science and Technology of China, Chengdu, China. ⁵Beijing National Laboratory for Condensed Matter Physics, Institute of Physics, Chinese Academy of Sciences, Beijing, China. ⁶DongFang Boiler Group Co., LTD, Chengdu, China. ⁷Graduate School of Human and Environmental Studies, Kyoto University, Sakyo-ku, Kyoto, Japan. ⁸Department of Physics, Technical University of Denmark, Kongens Lyngby, Denmark. ⁹X-ray Science Division, Advanced Photon Source, Argonne National Laboratory, Lemont, IL, USA. ¹⁰The Key Laboratory for Magnetism and Magnetic Materials, Lanzhou University, Lanzhou, China. ¹¹National Laboratory of Solid State Microstructures, Department of Physics and Collaborative Innovation Center of Advanced Microstructures, Nanjing University, Nanjing, China. ¹²State Key Laboratory of Advanced Technology for Materials Synthesis and Processing, School of Materials Science and Engineering, Wuhan University of Technology, Wuhan, China.

*Corresponding author. Email: kangyijin@scu.edu.cn (Y.K.); wag@caltech.edu (W.A.G.)

†These authors contributed equally to this work.

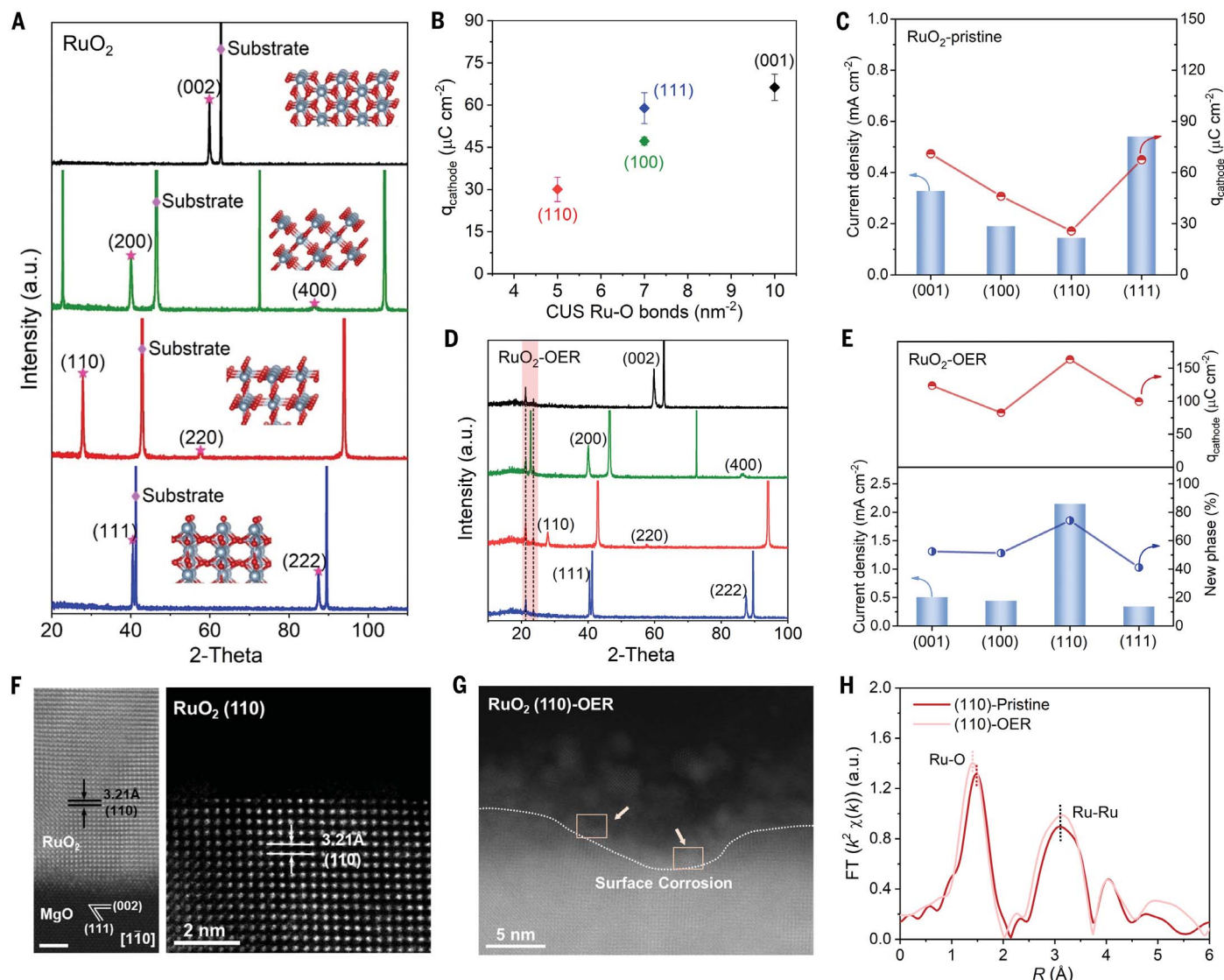


Fig. 1. Investigation on well-defined extended surfaces of RuO₂. (A) XRD patterns of thin films with selected orientations that expose RuO₂(001), RuO₂ (100), RuO₂ (110), and RuO₂ (111) surfaces, respectively. Red stars highlight the characteristic peaks for each orientation, and purple rhombuses highlight the peaks for substrate materials. Insets in (A) illustrate the structure for selected crystalline orientations. (B) The $q_{cathodic}^*$ for each orientation as a function of CUS Ru-O number. (C) Bar chart showing apparent current densities and the $q_{cathodic}^*$ for each surface. (D) XRD patterns for thin films after electrochemical activation, showing that a new phase evolves, as highlighted

in the shaded pink region. (E) Chart showing the correlation among activity (current density), $q_{cathodic}^*$, and the phase ratio for the thin films after activation. All current density bar charts are at 1.6 V versus a reversible hydrogen electrode (RHE). (F) Cross-sectional HAADF-STEM images of RuO₂(110) film, indicating that RuO₂ film grew epitaxially along the surface of MgO and terminated by a near atomically flat surface. Scale bar, 2 nm. (G) HAADF-STEM image of RuO₂(110) surface after OER test. (H) Fourier-transform (FT) extended x-ray absorption fine structure of RuO₂(110), obtained by grazing incidence x-ray absorption spectrum.

ratio of the new RuO₄ phase for each orientation in the XRD patterns to determine the extent of RuO₂ thin film evolution during OER. As shown in Fig. 1E, the current densities of RuO₂ after the activation process for different crystalline orientations correlated strongly with both the phase ratio and $q_{cathodic}^*$ (i.e., electrochemical surface area). The trend of $q_{cathodic}^*$ values to crystalline orientations was completely different from that of thin films before OER activation (compare Fig. 1C and Fig. 1E), indicating that the change in surface area was structure dependent.

We used aberration-corrected transmission electron microscope and synchrotron light source-based techniques to track the structure evolution of RuO₂ thin films during OER. Because RuO₂(110) exhibited the most drastic change in OER reaction among all the selected orientations, we chose it for the demonstration. Energy-dispersive spectroscopy (EDS) (fig. S5A) maps and high-angle annular dark-field scanning transmission electron microscopy (HAADF-STEM) (fig. S5B) of the cross-section of pristine RuO₂(110) film presented a highly crystalline and long-range ordered (110) plane

with 47 nm in thickness, which was consistent with results from XRR and XRD. Atomic-resolution HAADF-STEM (as shown in Fig. 1G) revealed that RuO₂(110) epitaxially grew on MgO (001) and terminated by an atomically flat surface.

Low-energy electron microscopy (fig. S6) revealed a uniform film morphology for RuO₂ (110), confirming the atomically flat surface. However, the film underwent severe corrosion during OER. Synchrotron XRR data-fitting results indicated that the roughness of RuO₂(110) surface changes from 1.3 nm for the pristine

film to 5.5 nm after OER (fig. S7, A and B, and table S3) with a drastic increase of q_{cathodic}^* suggesting a substantially increased population of active sites and surface reconstruction. Scattering-length density analysis (fig. S7C) demonstrated that an uneven and lower mass density layer formed on the (110) film after OER, which correlated with Ru leaching and severe surface reconstruction. XRD confirmed the existence of a new phase (fig. S8A).

We used grazing incidence diffraction (GID) as a surface-sensitive probe to identify the new phase as a species protruding out of the surface plane, most likely as high-valent Ru oxide clusters (fig. S8B). The broad peak width in XRD and GID suggested that this new structural phase had low crystallinity. Additionally, the substantially reduced intensities for RuO₂ (110), RuO₂(220), and MgO(004) in the GID pattern also imply the high epitaxial quality of the thin film samples (e.g., Bragg conditions for substrate and epitaxial film were not satisfied at the GID scattering geometry). Figure 1G and fig. S9 show the eroded surface structure of RuO₂(110) after OER, where surface corrosion accompanied with formation of polycrystalline and amorphous RuO_x species was observed.

We also found Ru sites transforming to disordered phases at many step sites (as shown in the pink box in fig. S9), implying that low-coordinated step sites might be the trigger points of continuous degradation. The surface species were further revealed with the help of grazing-incidence x-ray absorption spectrum (GIXAS). In the x-ray absorption near-edge structure spectra (fig. S10), the thin film after OER had a higher edge position and greater white-line intensity than the pristine film, which implies increased valence for Ru after OER. Fourier transform of the extended x-ray absorption fine structure revealed a slightly reduced Ru-O bond length for the film after OER (Fig. 1H), which corresponded to a shorter Ru-O bond (1.7 Å) of RuO₄ rather than that of RuO₂ (1.94 or 1.98 Å).

From the above experimental results, we concluded that under OER conditions, a fast and structure-dependent corrosion process started at the surface of RuO₂ electrocatalysts to produce high-valent Ru species and that this corrosion process activated RuO₂ toward OER through the substantially increased electrochemical surface area of the corroded surface. Although this corrosion improved the OER activity of RuO₂ initially through an apparent activation, the high Ru dissolution rate from corrosion leads to failure of the electrocatalyst in a relatively short period.

Ta-modified RuO₂

For practical application in the PEM-WE industry, the lifetime of the RuO₂ catalyst must be dramatically improved before RuO₂ can be used as an OER electrocatalyst. We explored

transition metal-modified RuO₂ materials for improved activity, stability, or both. We identified that Ta improved both the intrinsic activity and the chemical stability of RuO₂ catalysts.

We added Ta onto RuO₂ thin films through magnetron sputtering. Adding Ta atoms on the well-defined RuO₂ surface did not change the crystalline orientation, as shown by XRD (Fig. 2A and fig. S11). A slight increase in RMS roughness was observed on Ta-doped films through atomic force microscopy (fig. S12 and table S4). The cross-sectional HAADF-STEM image of TaRuO₂(110) film in Fig. 2B depicts a well-defined interface between the film and MgO(001) substrate and also a well-preserved and ordered (110) plane after Ta sputtering, confirming that Ta sputtering did not damage the film orientation.

The HAADF-STEM image in Fig. 2B also shows an ordered and near atomically flat surface lattice of TaRuO₂(110) film after Ta sputtering. The distance between the atoms highlighted with red circles and the subsurface Ru atoms (3.39 to ~3.40 Å) is larger than that of the adjacent atoms and the subsurface atoms (3.21 Å), which is likely caused by Ta atom occupation. The electron energy loss spectra (EELS) of surface atomic layers (Fig. 2C and fig. S13), marked with an orange box in Fig. 2B, showed a distinct signal at 1780 to ~1795 eV, which corresponds to the Ta-M₄ edge, whereas no EELS Ta signal was observed in the RuO₂ (110). The evidence above indicated that Ta atoms were successfully doped in the surface RuO₂ lattice after sputtering, whereas the surface orientation and flatness were nearly unchanged. X-ray photoelectron spectroscopy (fig. S14) of these Ta-doped films showed that the binding energy of Ta 4f is ~26.3 eV, revealing a +5 valence state of Ta on RuO₂ films. The amount of Ta doping is also detailed in table S5.

After the RuO₂ surface was modified by Ta atoms, the OER activity improved dramatically. Figure 2D and fig. S15 show the CV curves with iR correction for Ta-doped and pure RuO₂ films. Each Ta-doped film showed much larger current densities of OER compared with corresponding pure RuO₂ film. For example, Ta-RuO₂ (110) exhibited a geometric current density of 0.61 mA cm⁻² at 1.6 V versus reference hydrogen electrode (RHE), which was five-times higher than that of RuO₂ (110). Tafel plots in fig. S16 demonstrate that Ta-doped RuO₂ films showed lower Tafel slopes compared with pure RuO₂, namely 78.3 mV dec⁻¹ (where “dec” is “decade”) for Ta-RuO₂ (110) and 131.2 mV dec⁻¹ for RuO₂ (110), indicating that Ta-doped RuO₂ films had the faster kinetic rate of OER. We also studied the electrochemical impedance spectroscopy (EIS) to compare the rate of OER between Ta-doped and pure RuO₂ films. The Nyquist plots for Ta-doped and pure RuO₂ films at 1.6 V versus RHE are presented in

fig. S17. According to the fitting results (table S6), Ta-doped RuO₂ films exhibited much smaller charge transfer resistance (R_{ct}) compared with pure RuO₂ films, i.e., $R_{\text{ct}} = 478$ ohms for Ta-RuO₂ (110) and $R_{\text{ct}} = 3392$ ohms for RuO₂ (110), indicating that Ta-doped RuO₂ films provide faster charge transfer and rate of reaction toward OER. The change in capacitance charge over CV cycles under OER conditions was also greatly suppressed (fig. S18). Although the activities of pristine Ta-RuO₂ thin films with various crystalline orientations still correlated with the pseudocapacitive charge densities (fig. S19), this correlation was weaker than that for RuO₂ thin films, which implied that Ta changed the intrinsic activity of RuO₂, in addition to suppressing the morphology and structure evolution of electrocatalysts (fig. S20).

As shown in Fig. 2E, the surface of TaRuO₂ (110) thin films was less drastically changed after the OER test than that of RuO₂(110). EELS spectra of TaRuO₂(110) surface region (fig. S21) further verified that Ta remained in the surface lattice after the OER test, confirming the stronger structure stability of the Ta-doped RuO₂ surface. Accordingly, less new phase formation (high-valent Ru oxide species) was observed on Ta-modified RuO₂ thin films after OER (Fig. 2F). In situ and ex situ electrochemical Raman spectroscopy analysis (fig. S22) offered more evidence about degradation of RuO₂ and verified that Ta doping substantially improved the stability of RuO₂ films. We clearly observed the vibration modes of E_g (536 cm⁻¹), A_{1g} (649 cm⁻¹), and B_{2g} (715 cm⁻¹), which are ascribed to the featured modes of RuO₂ (110) under open circuit potential (OCP) in fig. S22A. Two distinct vibration modes also appeared around 428 cm⁻¹ and 594 cm⁻¹, which can be ascribed to the bond between Ru sites and hydroxyl intermediates (36). With increasing applied potentials, the vibration modes of E_g, A_{1g}, and B_{2g} exhibited apparent red shifts toward low wave number, while the vibration modes of Ru-OH remained unchanged. For example, the E_g mode showed a red shift from 536 cm⁻¹ to 524 cm⁻¹ when the applied potential reached 1.73 V versus RHE. The red shifts in peak position of RuO₂ (110) can be attributed to the formation of nano-sized clusters during OER (37), implying the reconstruction of RuO₂ (110) single-crystal film, which is consistent with our high-resolution transmission electron microscopy (HRTEM) results. Apart from the red shifts of vibration modes, the intensity of the E_g, A_{1g}, and B_{2g} modes of RuO₂ (110) dramatically decreased with increasing applied potentials. Specifically, the A_{1g} and B_{2g} modes of RuO₂ (110) almost disappeared when the potential reached 1.73 V versus RHE, showing the destruction of Ru-O configurations in RuO₂ (110) crystal structure during OER. The in situ Raman spectra of Ta-RuO₂ is illustrated in fig. S22B (110). The E_g, A_{1g}, and B_{2g} modes of Ta-RuO₂ (110) are

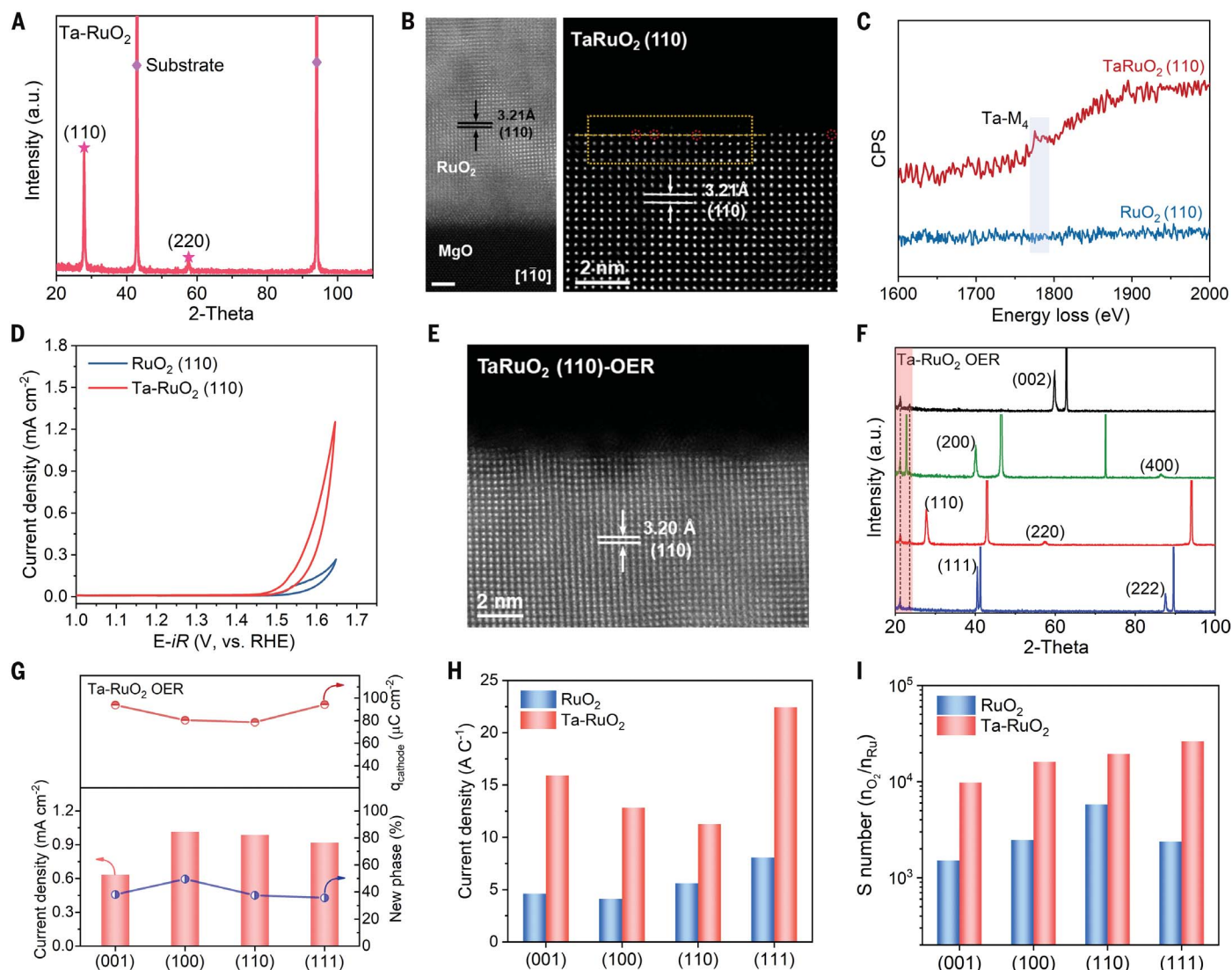


Fig. 2. Investigations on Ta-modified RuO₂ surfaces. (A) XRD pattern of Ta-doped RuO₂(110) thin film. Red stars highlight the characteristic peaks for RuO₂(110), and purple rhombuses highlight the peaks for the substrate material. (B) Cross-sectional HAADF-STEM images of Ta-doped RuO₂(110) film, indicating that Ta sputtering does not damage the film orientation or crystallization. Scale bar, 2 nm. (C) EELS spectra of Ta-M₄ edge. CPS, counts per second. (D) CV curves of RuO₂(110) and Ta-RuO₂(110). (E) HAADF-STEM image of TaRuO₂(110) surface

after OER test. (F) XRD patterns for thin films after electrochemical activation, showing that a new phase evolves, as highlighted. (G) Chart showing the correlation among activity (current density), q_{cathodic}^* , and the phase ratio for the thin films after activation. (H) Bar chart showing current densities normalized by q_{cathodic}^* to represent intrinsic activities. (I) Bar chart showing the thin film S number, which is defined as the molar ratio of O₂ produced to dissolved Ru, representing the stability of electrocatalysts. All bar charts show current density at 1.6 V versus RHE.

located at 537 cm⁻¹, 649 cm⁻¹, and 716 cm⁻¹ under OCP, respectively, which are similar to that of pure RuO₂(110). The vibration of Ru-OH also appeared around 429 cm⁻¹ and 594 cm⁻¹. Compared with the apparent changes in Raman spectra of RuO₂(110) during OER, Ta-RuO₂(110) showed few variations in Raman signals with increasing applied potentials. The E_g mode of Ta-RuO₂(110) stayed at 537 cm⁻¹ under all the applied potentials in our experiments, which shows that doping Ta noticeably prevents the RuO₂(110) surface from reconstruction and suppresses the destruction of RuO₂ crystal structure. Considering the strong fluorescence below 300 cm⁻¹ under in situ conditions, we

carried out ex situ Raman characterizations (as shown in fig. S22, C and D). We found similar red shifts for the E_g, A_{1g}, and B_{2g} modes of RuO₂(110) after OER (fig. S22C). Moreover, a distinct Raman peak appeared around 229 cm⁻¹, which is ascribed to RuO₄ configurations (38) on RuO₂(110) film after OER (fig. S22C). This observation implies the formation of high-valent Ru species on RuO₂ films, which is consistent with the XRD and GIXAS results in Fig. 1. However, we observed neither the red shifts of vibration modes nor the vibrations of RuO₄ on Ta-RuO₂(110) after OER (fig. S22D). Although the activities of Ta-RuO₂ still correlated with both RuO₄ phase ratio and capacitance charge

(Fig. 2G), the correlation for Ta-RuO₂ no longer followed the same trend seen in RuO₂ (fig. S23). After normalizing the current densities by the corresponding q_{cathodic}^* to reflect the intrinsic OER activities (Fig. 2H), Ta doping was shown to improve the intrinsic activity of RuO₂ toward OER.

The stability of RuO₂ and Ta-RuO₂ was quantified by measuring Ru dissolution under continuous operation of OER at 1.6 V, as determined by inductively coupled plasma mass spectrometry (ICP-MS). The Ru dissolution rates for respective crystal faces were 11.9 (001), 5.3 (100), 44.5 (110), and 5.7 (111) ng hour⁻¹ for RuO₂, and 3.9 (001), 2.4 (100), 21.8 (110), and

2.4 (111) ng hour⁻¹ for Ta-RuO₂, respectively (figs. S24 and S25). This trend of Ru dissolution in RuO₂ was consistent with previous reports. (39) However, the Ta modification suppressed Ru dissolution in RuO₂ electrocatalysts. The *S* number, (*#*0) which is defined as the molar ratio of O₂ produced to dissolved Ru, is calculated and presented in Fig. 2I, illustrating the much-improved activity and stability of RuO₂ electrocatalyst resulting from Ta doping.

Computational studies

We performed a series of QM calculations to provide insight into the atomistic origin of the improved intrinsic activity and stability of RuO₂ from Ta incorporation. We found that the (110) surface led to the most drastic change during the apparent activation, whereas (100) led to the least drastic change. Here we used the GCQM method (31) to compare the activity of (110) and (100) surfaces as a function of applied potential with and without surface Ta doping. The atomic surface geometries and distinctive surface sites for RuO₂ (100) and (110) facets are shown in figs. S26, A and B.

Under electrochemical conditions, applying anodic polarization led to the successive oxidation of the surface state. Starting from the surface fully covered by hydroxyl groups, we constructed the surface free-energy diagrams for pure RuO₂ (fig. S26, C and D). The surfaces are saturated by bridge oxo (μ_2 -O) and by terminal oxo (μ_1 -O) at the potential of 1.31 V for RuO₂(100) and at the potential of 1.21 V versus RHE for RuO₂(110), implying the facile surface oxidation on the RuO₂ surface. For Ta-RuO₂, we found that Ta preferentially doped at the surface on RuO₂(100) (fig. S27), where only CUS sites were present. The Ta-RuO₂ (100) surface showed a dominant Ta-OH state even at a high potential (fig. S26E). However, although Ta preferred the surface bridge site (BRI) over the CUS site (fig. S28), we focused on the role of Ta at the CUS because the Ta at the BRI site was not only directly involved in the OER pathway but also decreased OER activity (fig. S29). For Ta-RuO₂(110) with Ta_{CUS}, the hydroxyl on Ta (μ_1^{Ta} -OH) was slightly more favorable than the terminal oxo (μ_1^{Ta} -O) at potentials up to 1.65 V versus RHE, indicating a higher population of μ_1^{Ta} -OH (fig. S26F).

The reaction mechanism for OER on RuO₂ (100) is shown in Fig. 3A. A surface H₂O molecule reacted with the μ_1 -O to make a new O-O bond forming μ_1 -OOH (state 2) and simultaneously transferred its H to an adjacent μ_2 -O to form μ_2 -OH. This reaction had a reaction free energy (ΔG) of 0.40 eV and a free-energy barrier, ΔG^\ddagger , of 0.77 eV at 1.6 V versus RHE (Fig. 3B). After making μ_1 -OOH, the successive exothermic deprotonation and O₂/H₂O exchange steps returned the surface back to state 1. On Ta-RuO₂(100), the proton was transferred to μ_1^{Ta} -OH rather

than μ_2 -O during O-O bond formation, which led to formation of μ_1^{Ta} -H₂O and μ_1 -OOH on Ru (Fig. 3A, bottom). This reaction had a 0.07-eV-lower ΔG^\ddagger of 0.70 eV at 1.6 V versus RHE compared with RuO₂(100) (Fig. 3B).

On the RuO₂(110) surface, although the μ_2 -O was a stronger proton acceptor (fig. S26D and S30), the kinetic barrier of the water dissociation step transferring the proton to μ_1 -O had a 0.09-eV-lower barrier of 0.78 eV at 1.6 V versus RHE. The Ta doping at CUS leads to much more favorable water dissociation with $\Delta G^\ddagger = 0.57$ eV and $\Delta G = 0.30$ eV at 1.6 V versus RHE (Fig. 3C).

To predict the current density, we calculated the turnover frequency (TOF) by assuming that the O-O coupling step is the rate-determining step (supplementary text). We predicted that RuO₂(100) had a 1.8-fold higher TOF of 0.69 s⁻¹ compared with RuO₂(110), with a TOF of 0.36 s⁻¹ (Fig. 3D). This analysis led to a current density of 0.32 mA cm⁻² for RuO₂(100) and 0.12 mA cm⁻² for RuO₂(110) (fig. S31), which was consistent with our experiments (Fig. 1C and fig. S4E). The Ta doping on RuO₂(100) led to a TOF of 5.62 s⁻¹ at 1.6 V versus RHE, which was 8.1-fold faster than pure RuO₂(100). This analysis led to a current density of 0.69 mA cm⁻², which was more than two times higher than that of pure RuO₂(100), for a doping concentration of 8.9%, which again agreed very well with our experiment in which the Ta-doped RuO₂ (100) had a current density two times higher than that of pure RuO₂ (Fig. 2H).

We predicted that Ta doping on RuO₂(110) could have dramatic effects. The TOF near the Ta_{CUS} was calculated as 382 s⁻¹ at 1.6 V versus RHE, which is 1000 times faster than for pure RuO₂(110). However, this Ta_{CUS} was thermodynamically less stable than Ta_{BRI}. Therefore, there may be only trace amounts of this phase present. We estimate that the presence of only 0.04 atomic % (at %) of surface Ta_{CUS} could lead to a current density 1.8 times higher than that of pure RuO₂(110), as observed in our experiment (Fig. 2H).

To provide a theoretical explanation for the enhanced durability of Ta-RuO₂ at OER working conditions, we calculated the energetics of the dissolution process. Based on our experiment, we conclude that the corrosion most likely involves the high-valent Ru clusters (figs. S8 to S10). Using *ab initio* molecular dynamics, Klyukin *et al.* suggested that Ru dissolution occurs through deprotonation of the RuO₂(OH)₂ cluster (34). Because corrosion occurs mainly at the defect site (41), we built a high-index (231) surface model of rutile structure (fig. S32A) that exposed the (110) surface with the [111] step edge having the alternative two metal sites, M_{BRI} and M_{CUS} (fig. S32B). There were three distinctive μ_1 -O motifs to bind the cluster on the edge. One motif was bonded to M_{BRI} (M_{BRI}-O), and the other two motifs

were bonded to M_{CUS}, which were either parallel (M_{CUS}-O⁻) or perpendicular (M_{CUS}-O⁺) to the (110) terrace plane.

We calculated the energetics of the RuO₂(OH)₂ oxidation on these different binding sites, which led to Ru dissolution (34). Figure 3E (top) shows the representative oxidation process on the Ru_{CUS}-O⁺ site on pure RuO₂, and the energies are shown in Fig. 3F. The reaction energies of the deprotonation of RuO₂(OH)₂ complex (ΔG^{1st}) were 0.97 eV, 1.04 eV, and 1.28 eV for the Ru_{BRI}-O, Ru_{CUS}-O⁻, and Ru_{CUS}-O⁺ sites, respectively (table S7). The deprotonation led to the bond-length increase between Ru in the cluster and μ_1 -O (d_{Ru-O}), leading to the RuO₃OH detachment except for the bond at Ru_{BRI}-O sites, which still maintained a chemical bonding with d_{Ru-O} of 2.00 Å. However, the following second deprotonation led to Ru dissolution without exception (table S8), with much lower energy (ΔG^{2nd}), which is in agreement with the previous study (34).

To investigate the role of Ta dopant on durability, we built corresponding (231) surfaces with different doping sites, Ta_{CUS} (fig. S32C) and Ta_{BRI} (fig. S32D). Although the Ta dopant still preferred the CUS site over BRI sites on the edge by -0.81 eV on the intact edge structure, we noted that the Ta_{CUS} was stabilized by the binding of the RuO₂(OH)₂ cluster. This strong interaction left the cluster with even lower energy by 0.39 eV for Ta_{CUS}-O⁺ and 0.11 eV for Ta_{CUS}-O⁻ sites compared with the Ta_{BRI} counterparts. The ΔG_1 for the deprotonation of the intermediate were 1.25 eV for Ta_{CUS}-O⁺ and 1.26 eV Ta_{CUS}-O⁻, which were higher by 0.28 eV and 0.22 eV compared with the corresponding cases on pure RuO₂(231) facets. Moreover, the oxidized intermediate, RuO₃OH, still formed a chemical bond to the μ_1 -O with a d_{Ru-O} of 1.93 Å for Ta_{CUS}-O⁺ and 1.83 Å for Ta_{CUS}-O⁻. The ΔG_2 values toward RuO₄ dissolution of 1.16 eV and 1.05 eV, respectively, were 0.74 and 0.77 eV higher than that on pure RuO₂. We could not find such a stability increase of the bound intermediate with Ta doping on the BRI site (table S7), suggesting that the strong binding of the Ru dissolution intermediate on Ta_{CUS}-O enhanced the durability of the Ta-RuO₂ catalyst in the working condition.

Demonstration of Ta-RuO₂ for industrial water electrolysis

Based on what we learned from studying the above well-defined extended surfaces, we implemented the synthesis of nanoparticulate Ta-RuO₂ electrocatalysts and applied them in an industrial environment to demonstrate Ta-RuO₂ as a practical electrocatalyst for industrial water electrolysis. Such Ta-RuO₂ electrocatalysts have been commercialized, mass produced, and are available on the market. We synthesized the nanoparticulate Ta-RuO₂ materials through a modified sol-gel method.

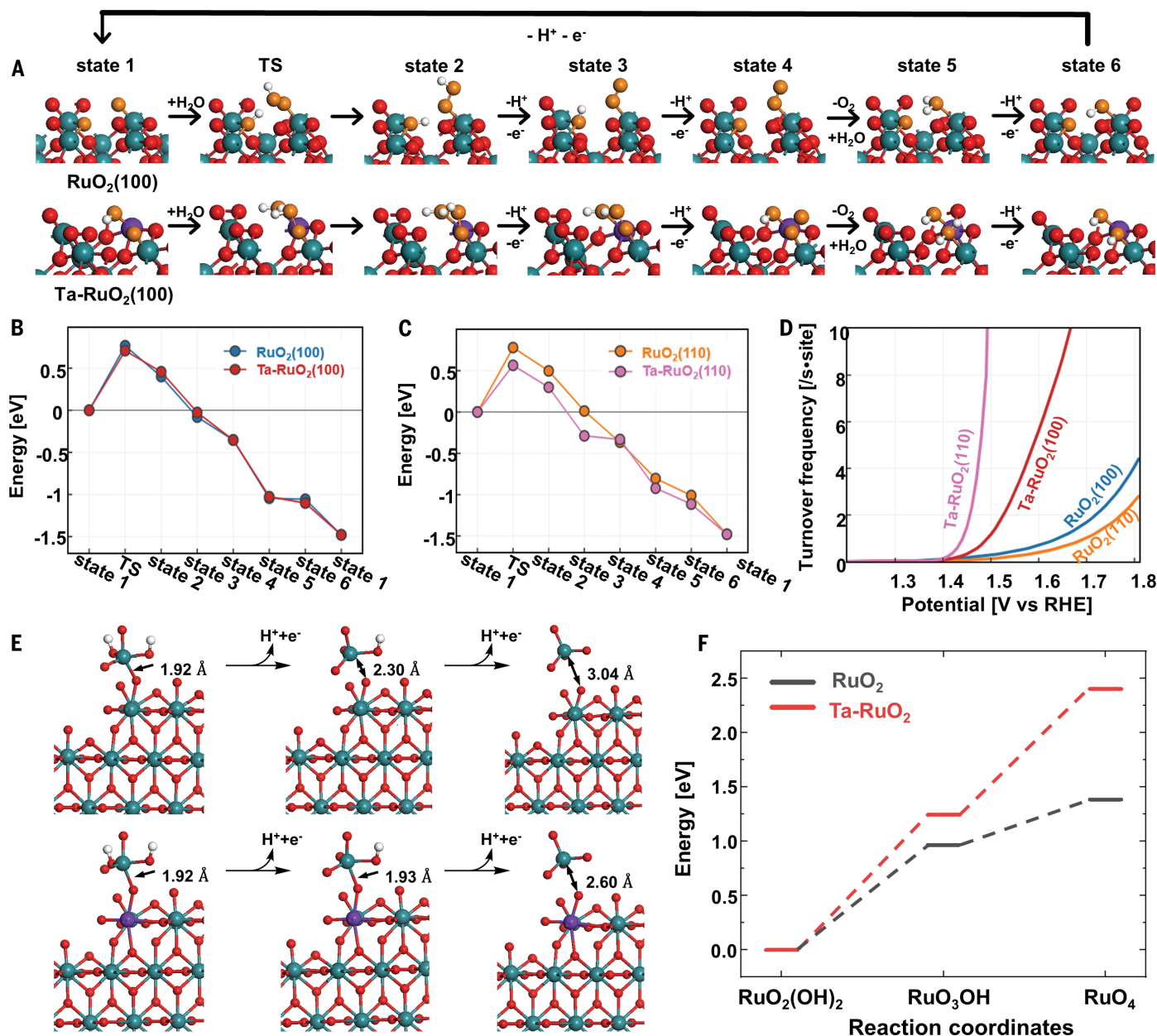


Fig. 3. OER reaction mechanisms over RuO_2 and Ta-doped RuO_2 . **(A)** The OER pathway on pure $\text{RuO}_2(100)$ and Ta-doped $\text{RuO}_2(100)$. TS denotes the transition state. The proton is transferred to a terminal oxo during the water dissociation step except for the pure $\text{RuO}_2(100)$. The purple, turquoise, red, orange, and white spheres denote Ta, Ru, O, and H atoms, respectively. The free-energy landscapes along the OER reaction coordinates on the **(B)** (100) surface and **(C)** (110) surface. The blue, red, yellow, and pink colors represent the pure RuO_2 (100), Ta-doped $\text{RuO}_2(100)$,

pure RuO_2 (110), and Ta-doped RuO_2 (110), respectively. **(D)** Turnover frequency (TOF) on the four model surfaces. **(E)** Ru dissolution on the step edge of the RuO_2 and Ta-doped RuO_2 (231) surface. The serial oxidation of Ru dissolution intermediate, $\text{RuO}_2(\text{OH})_2$, bound to the edge CUS site through $\mu_1\text{-O}^-$ is depicted on pure RuO_2 (top) and on Ta-RuO_2 (bottom). **(F)** The potential energy landscape during the two sequential deprotonations, which shows that the Ru dissolution on Ta-RuO_2 requires more energy compared with pure RuO_2 .

(24, 42) A mixture of ruthenium chloride and tantalum chloride in ethanol solution was precipitated by alginate. The formed gel was subsequently dried and then calcined in air to produce ruthenium-based oxides (see materials and methods for details). Such synthesis could be readily scaled up to kilogram production, as we are currently doing to supply the commercialized Ta-RuO_2 catalyst products. The Ta

content in Ta-RuO_2 is tunable, with the nanomaterials obtained denoted as $\text{Ta}_x\text{Ru}_{1-x}\text{O}_{2-x}$. As a control for comparison purposes, a RuO_{2-x} sample was also synthesized by the same method but with no Ta added.

As confirmed by XRD (fig. S33A), doping RuO_2 with Ta did not change the rutile structure of RuO_2 , at least for up to 20 at % Ta. As shown in the TEM image (fig. S33B), $\text{Ta}_{0.1}\text{Ru}_{0.9}\text{O}_{2-x}$

exhibited a porous and rough surface morphology, which provides a high surface area to make more OER active sites available. Figure 4A shows a high-resolution HRTEM image for a projection of the $\text{Ta}_{0.1}\text{Ru}_{0.9}\text{O}_{2-x}(001)$ plane in which the interplanar distances were 3.30 Å for (110) and 2.32 Å for (200), which is consistent with the XRD data. Element mapping enabled by EDS indicates that Ru, Ta,

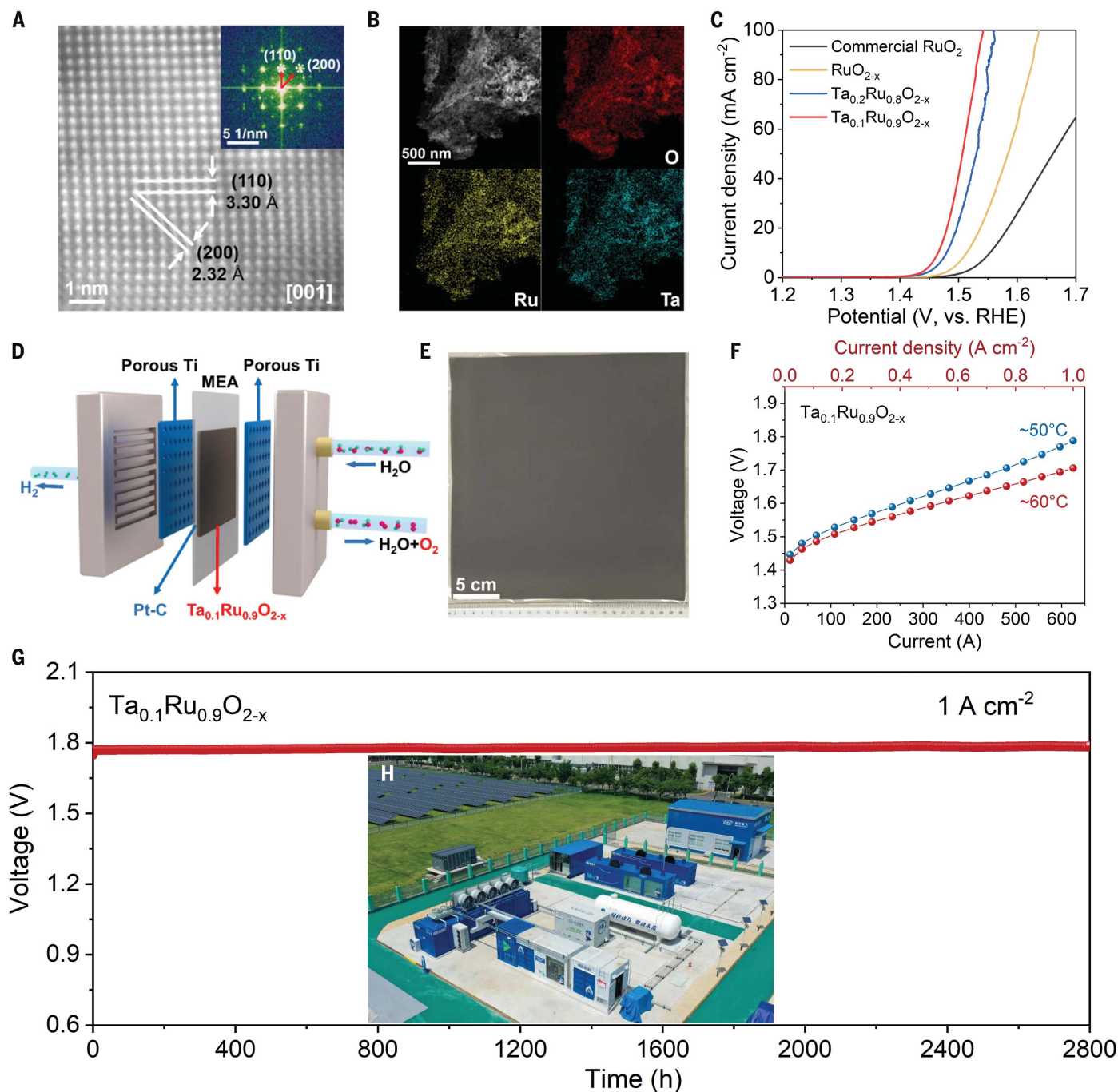


Fig. 4. Nanosized $\text{Ta}_{0.1}\text{Ru}_{0.9}\text{O}_{2-x}$ electrocatalyst in industrial testing. (A) HRTEM image (inset: fast Fourier transform pattern) and (B) EDS mapping of $\text{Ta}_{0.1}\text{Ru}_{0.9}\text{O}_{2-x}$. (C) OER curves of $\text{Ta}_{0.1}\text{Ru}_{0.9}\text{O}_{2-x}$, $\text{Ta}_{0.2}\text{Ru}_{0.8}\text{O}_{2-x}$, RuO_{2-x} , and commercial RuO_2 powder. (D) Illustration of a single-cell PEM-WE. (E) Photograph and (F) I - V curves of a 625-cm 2 MEA using $\text{Ta}_{0.1}\text{Ru}_{0.9}\text{O}_{2-x}$. (G) Voltage-time curves of PEM-WE with $\text{Ta}_{0.1}\text{Ru}_{0.9}\text{O}_{2-x}$. (H) A demonstration project in which solar-powered hydrogen production (of up to megawatt outputs) directly feeds a hydrogen refueling station.

and O were homogeneously distributed in $\text{Ta}_{0.1}\text{Ru}_{0.9}\text{O}_{2-x}$ (Fig. 4B). More characterizations can be found in figs. S34 to S38.

Figure 4C shows the results of OER evaluation on a rotating-disc electrode in 0.5 M H_2SO_4 electrolyte. From the OER polarization curves, $\text{Ta}_{0.1}\text{Ru}_{0.9}\text{O}_{2-x}$ shows a low overpotential of 226 mV at 10 mA cm^{-2} , appearing to have better OER activity performance over $\text{Ta}_{0.2}\text{Ru}_{0.8}\text{O}_{2-x}$

(fig. S39), synthesized RuO_{2-x} (fig. S40A), and commercially available RuO_2 powder (fig. S40B). The Tafel plots for $\text{Ta}_{0.1}\text{Ru}_{0.9}\text{O}_{2-x}$ together with the benchmark samples are depicted in fig. S41A. The representative $\text{Ta}_{0.1}\text{Ru}_{0.9}\text{O}_{2-x}$ again outperformed other samples, exhibiting a low Tafel slope of 47.1 mV dec^{-1} , which is much smaller than that of commercial RuO_2 . We evaluated the intrinsic activities of $\text{Ta}_{0.1}\text{Ru}_{0.9}\text{O}_{2-x}$

on the basis of TOFs at different overpotentials (fig. S41B). We found that the TOF of $\text{Ta}_{0.1}\text{Ru}_{0.9}\text{O}_{2-x}$ reached 0.086 s^{-1} at an overpotential of 280 mV, which is the highest among the benchmark samples and 20 times higher than that of commercial RuO_2 (0.004 s^{-1}). The Nyquist plots shown as fig. S41C demonstrate that $\text{Ta}_{0.1}\text{Ru}_{0.9}\text{O}_{2-x}$ presented a smaller R_{ct} compared with other samples, which implies that

Ta_{0.1}Ru_{0.9}O_{2-x} exhibited faster charge transfer toward OER. These results placed Ta_{0.1}Ru_{0.9}O_{2-x} among the best catalysts in our controlled experiments.

To further illustrate the intrinsic OER activity for each electrocatalyst material, the apparent current density was also normalized to specific activity based on double-layer capacitance, C_{dl} (fig. S42 and table S9). We found that Ta_{0.1}Ru_{0.9}O_{2-x} and Ta_{0.2}Ru_{0.8}O_{2-x} had similar specific activities, both outperforming RuO_{2-x} and commercial RuO₂ (fig. S43). Notably, the Ta_{0.1}Ru_{0.9}O_{2-x} powder catalyst exhibited a prominent S number, which is within the same order of magnitude as that of IrO₂, showcasing the excellent stability of Ta_{0.1}Ru_{0.9}O_{2-x} (fig. S44). We note that simply mixing Ta₂O₅ and RuO₂ led to only slightly improved OER activity (29) (fig. S45). We made similar observations for the thin film case (fig. S46) in which Ta₂O₅ was deposited on top of RuO₂ thin films through physical vapor deposition: This Ta₂O₅-modified RuO₂ (110) thin film had activity similar to that of RuO₂(110), and the drastic evolution during OER cycles was not suppressed.

We used Ta_{0.1}Ru_{0.9}O_{2-x} electrocatalyst in MEAs (Fig. 4D). Current-voltage relation (I - V) curves demonstrate that MEAs with Ta_{0.1}Ru_{0.9}O_{2-x} anode catalyst required 109 and 330 mV less in voltage to reach 1 A cm⁻² than did commercial RuO₂ and IrO₂ catalysts, respectively (fig. S47A), which implied that the MEA with Ta_{0.1}Ru_{0.9}O_{2-x} had higher efficiency for water electrolysis. Ta_{0.1}Ru_{0.9}O_{2-x} was further used as the anode catalyst to fabricate the industrial MEA as large as 25 cm by 25 cm (i.e., 625 cm² as shown in Fig. 4E). A single-cell water electrolyzer (fig. S48) enabled electrolyzing current as large as 625 A at voltage as low as 1.704 V (Fig. 4F), delivering a rated power of 1 kW and a hydrogen production rate at 0.523 normal cubic meters (Nm³) hour⁻¹ (i.e., 145 ml s⁻¹ or 23.35 mol hour⁻¹).

During operation at a current density of 1 A cm⁻², Ta_{0.1}Ru_{0.9}O_{2-x} exhibited a constant working voltage for at least 2800 hours at a decay rate <~14 μV hour⁻¹ (Fig. 4G), whereas RuO₂ lasted less than 50 hours before hitting the 2-V cutoff voltage (fig. S47B). This Ru-based electrocatalyst can be stably operated at a current density as high as 1 A cm⁻² in an MEA at industrial scale. As a demonstration project, the infrastructure for hydrogen production has been created and is integrated with solar-powered PEM-WE with outputs of up to megawatt rates, together with hydrogen storage and

a hydrogen refueling station (Fig. 4H). Although the Ta-RuO₂ electrocatalyst is still being further evaluated in the industrial environment, we have no doubt that it will play an important part in the water electrolysis industry.

Conclusions

We observed a structure-dependent corrosion on RuO₂ electrocatalysts during the OER process. Such corrosion is directly responsible for the poor stability (i.e., dissolution of Ru) of RuO₂ electrocatalysts. Ta doping suppresses the dissolution of Ru, while increasing the intrinsic activity of RuO₂ electrocatalysts toward OER. The industrial demonstration clearly shows that the poor stability issue of RuO₂ electrocatalysts has been successfully addressed and that Ru-based catalysts have more desirable OER activity than Ir-based catalysts, thus offering a highly attractive option for the electrocatalyst in PEM-WE.

REFERENCES AND NOTES

- V. R. Stamenkovic, D. Strmcnik, P. P. Lopes, N. M. Markovic, *Nat. Mater.* **16**, 57–69 (2016).
- N. S. Lewis, D. G. Nocera, *Proc. Natl. Acad. Sci. U.S.A.* **103**, 15729–15735 (2006).
- J. Song et al., *Chem. Soc. Rev.* **49**, 2196–2214 (2020).
- A. Buttler, H. Spliethoff, *Renew. Sustain. Energy Rev.* **82**, 2440–2454 (2018).
- M. Carmo, D. L. Fritz, J. Mergel, D. Stolten, *Int. J. Hydrogen Energy* **38**, 4901–4934 (2013).
- L. An et al., *Adv. Mater.* **33**, e2006328 (2021).
- K. E. Ayers et al., *ECS Trans.* **33**, 3–15 (2010).
- Y.-R. Zheng et al., *Nat. Energy* **7**, 55–64 (2022).
- Y. Chen et al., *Sci. Adv.* **7**, eabk1788 (2021).
- F. Cheng et al., *Nat. Chem.* **3**, 79–84 (2011).
- Y. Lin et al., *Nat. Commun.* **10**, 162 (2019).
- C. Liu et al., *Nat. Catal.* **4**, 36–45 (2021).
- Y. Qin et al., *Nat. Commun.* **13**, 3784 (2022).
- L. C. Seitz et al., *Science* **353**, 1011–1014 (2016).
- S. Hao et al., *Nat. Commun.* **11**, 5368 (2020).
- Z.-F. Huang et al., *Nat. Energy* **4**, 329–338 (2019).
- Y. Wen et al., *J. Am. Chem. Soc.* **143**, 6482–6490 (2021).
- Y. Yao et al., *Nat. Catal.* **2**, 304–313 (2019).
- B. Zhang et al., *Science* **352**, 333–337 (2016).
- L. Zhang et al., *Adv. Mater.* **32**, e2002297 (2020).
- P. C. K. Vesborg, T. F. Jaramillo, *RSC Adv.* **2**, 7933–7947 (2012).
- J. Kibsgaard, I. Chorkendorff, *Nat. Energy* **4**, 430–433 (2019).
- H. Over, *Chem. Rev.* **112**, 3356–3426 (2012).
- M. Retuerto et al., *Nat. Commun.* **10**, 2041 (2019).
- S.-C. Sun et al., *Angew. Chem. Int. Ed.* **61**, e202202519 (2022).
- J. Wang et al., *Chem* **8**, 1673–1687 (2022).
- A. Zagalskaya, V. Alexandrov, *ACS Catal.* **10**, 3650–3657 (2020).
- K. A. Stoerzinger et al., *ACS Energy Lett.* **2**, 876–881 (2017).
- V. Natarajan, S. Basu, *Int. J. Hydrogen Energy* **40**, 16702–16713 (2015).
- Z. Yan et al., *Electrochim. Acta* **157**, 345–350 (2015).
- Y. Huang, R. J. Nielsen, W. A. Goddard 3rd, *J. Am. Chem. Soc.* **140**, 16773–16782 (2018).
- L. D. Burke, O. J. Murphy, *J. Electroanal. Chem. Interfacial Electrochem.* **96**, 19–27 (1979).
- K. A. Stoerzinger, L. Qiao, M. D. Biegalski, Y. Shao-Horn, *J. Phys. Chem. Lett.* **5**, 1636–1641 (2014).

- K. Klyukin, A. Zagalskaya, V. Alexandrov, *J. Phys. Chem. C Nanomater. Interfaces* **123**, 22151–22157 (2019).
- R. Kötz, S. Stucki, D. Scherson, D. M. Kolb, *J. Electroanal. Chem. Interfacial Electrochem.* **172**, 211–219 (1984).
- H. C. Jo, K. M. Kim, H. Cheong, S.-H. Lee, S. K. Deb, *Electrochem. Solid-State Lett.* **8**, E39 (2005).
- A. V. Korotcov, Y.-S. Huang, K.-K. Tiong, D.-S. Tsai, *J. Raman Spectrosc.* **38**, 737–749 (2007).
- M. Naji et al., *J. Raman Spectrosc.* **46**, 661–668 (2015).
- C. Roy et al., *ACS Energy Lett.* **3**, 2045–2051 (2018).
- S. Geiger et al., *Nat. Catal.* **1**, 508–515 (2018).
- T. Weber et al., *ACS Catal.* **9**, 6530–6539 (2019).
- J. Kim, X. Yin, K.-C. Tsao, S. Fang, H. Yang, *J. Am. Chem. Soc.* **136**, 14646–14649 (2014).
- W. A. Goddard III, S. Kwon, DFT Geometry and Energy, Version 1.0.0, Zenodo (2024); <https://www.doi.org/10.5281/zenodo.14048116>.

ACKNOWLEDGMENTS

Funding: This work is primarily supported by Y.K.'s personal funds and resources, through Tianrui Technology Co., LTD. Computational work was supported by the Liquid Sunlight Alliance—which is supported by the US Department of Energy (DOE), Office of Science, Office of Basic Energy Sciences, Fuels from Sunlight Hub under award no. DE-SC0021266 (W.A.G.) and by an individual fellowship from the Resnick Sustainability Institute at Caltech (S.K.)—and used Stampede3 at Texas Advanced Computing Center through allocation DMR160114 from the Advanced Cyberinfrastructure Coordination Ecosystem: Services & Support (ACCESS) program, which is supported by NSF grants 2138259, 2138286, 2138307, 2137603, and 2138296 (W.A.G.). This research used beamline 33-ID-D of the Advanced Photon Source, a DOE Office of Science user facility operated for the DOE Office of Science by Argonne National Laboratory under contract no. DE-AC02-06CH11357. This research used beamline 4-ID of the National Synchrotron Light Source II, a DOE Office of Science User Facility operated for the DOE Office of Science by Brookhaven National Laboratory under contract no. DE-SC0012704. **Author contributions:** Y.K. provided all the resources through Tianrui Tech and supervised the project. J.Z. and Y.K. designed the experiment. J.Z. and X.F. performed the synthesis, characterization, and electrochemical tests. S.K. and W.A.G. carried out the theoretical calculations. K.C., L.Q., X.F., and Y.L. prepared the thin-films. X.L., F.X., J.W. and D.S. performed electron microscopy. J.Y. and H.S. facilitated the industrial tests. Y.W., T.U., Y.U., S.L., Y.L. and H.Z. are beam scientists who assisted in spectroscopy. G.C. performed the low energy electron microscopy. Y.K., J.Z., S.K., and W.A.G. drafted the manuscript. All authors discussed the results and wrote the paper. **Competing interests:** Y.K. through Tianrui Tech Co., LTD, commercialized the electrocatalysts described herein and holds the related patents. DongFang Boiler Group Co., LTD, is a megawatt water electrolyzer manufacturer and an energy solution provider. **Data and materials availability:** All data needed to evaluate the conclusions in the paper are present in the paper or the Supplementary Materials. The DFT data are available at Zenodo (43). **License information:** Copyright © 2025 the authors, some rights reserved; exclusive licensee American Association for the Advancement of Science. No claim to original US government works. <https://www.science.org/about/science-licenses-journal-article-reuse>

SUPPLEMENTARY MATERIALS

science.org/doi/10.1126/science.ado9938
Materials and Methods
Supplementary Text
Figs. S1 to S48
Tables S1 to S13
Movie S1
References (44–73)

Submitted 5 March 2024; resubmitted 20 August 2024
Accepted 22 November 2024
10.1126/science.ado9938